J Mater Sci (2006) 41:7814–7823
DOI 10.1007/s10853-006-0664-9

Nanoscale precipitation and mechanical properties of Al-0.06 at.% Sc alloys microalloyed with Yb or Gd

Marsha E. van Dalen · David C. Dunand · David N. Seidman

Received: 31 March 2006 / Accepted: 10 July 2006 / Published online: 24 October 2006

Abstract Dilute Al-0.06 at.% Sc alloys with microalloying additions of 50 at. ppm of ytterbium (Yb) or gadolinium (Gd) are studied with 3D local-electrode atom-probe (LEAP) tomography for different aging times at 300 °C. Peak-aged alloys exhibit $Al_3(Sc_{1-x}Yb_x)$ or $Al_3(Sc_{1-x}Gd_x)$ precipitates ($L1_2$ structure) with a higher number density (and therefore higher peak hardness) than a binary Al-0.06 at.% Sc alloy. The Al–Sc–Gd alloy exhibits a higher number density of precipitates with a smaller average radius than the Al–Sc–Yb alloy, leading to a higher hardness. In the Al–Sc–Gd alloy, only a small amount of the Sc is replaced by Gd in the $Al_3(Sc_{1-x}Gd_x)$ precipitates, where $x = 0.08$. By contrast, the hardness incubation time is significantly shorter in the Al–Sc–Yb alloy, due to the formation of Yb-rich $Al_3(Yb_{1-x}Sc_x)$ precipitates to which Sc subsequently diffuses, eventually forming Sc-rich $Al_3(Sc_{1-x}Yb_x)$ precipitates. For both alloys, the precipitate radii are found to be almost constant to an aging time of 24 h, although the concentration and distribution of the RE elements in the precipitates continues to evolve temporally. Similar to microhardness at ambient temperature, the creep resistance at 300 °C is significantly improved by RE microalloying of the binary Al-0.06 at.% Sc alloy.

M. E. van Dalen (✉) · D. C. Dunand · D. N. Seidman
Department of Materials Science and Engineering, Northwestern University, 2220 Campus Dr., Evanston, IL 60208-3108, USA
e-mail: vandalen@northwestern.edu

D. N. Seidman
Northwestern University Center for Atom-Probe Tomography (NUCAPT), Evanston, IL, USA

Introduction

Dilute, coarse-grained Al–Sc alloys show promise as castable, creep-resistant alloys due to the formation of a high number density of Al_3Sc precipitates, which coarsen slowly up to about 300 °C (corresponding to a homologous temperature of 0.61) [1–6]. Different ternary additions have been shown to improve the strength of binary Al–Sc alloys, including Mg for solid-solution strengthening at ambient and elevated temperatures [2, 7, 8] and Zr [9–16] or Ti [17] for increased coarsening resistance at high temperatures, important for retention of creep strength. Rare-earth (RE) elements are attractive ternary additions because: (i) many RE elements substitute for Sc in the Al_3Sc precipitates forming $Al_3(Sc_{1-x}RE_x)$ ($L1_2$ structure) with a high solubility, thereby replacing the more expensive Sc [18, 19]; (ii) the light RE elements have a smaller diffusivity in Al than Sc [20], improving the coarsening resistance of the precipitates; (iii) however, both the light RE elements and ytterbium (Yb) have a larger diffusivity in Al [20] than Zr or Ti [21], so that the RE atoms are incorporated into the $L1_2$ precipitates with faster kinetics than the Zr or Ti atoms; and (iv) unlike Ti or Zr [22], RE elements increase the lattice parameter mismatch between α-Al and $Al_3(Sc_{1-x},RE_x)$ [18, 19], which could increase the creep resistance of the alloy [23].

Sawtell and Morris [24, 25] studied Al-0.3 at.% Sc-0.3 at.% RE alloys (with RE = Er, Gd, Ho, or Y), where both Sc and the RE elements exceeded their maximum equilibrium solid-solubility, which, in the binary alloys, occurs at the eutectic temperatures of 639–655 °C for the various RE elements and 660 °C for Sc [26]. The samples were chill-cast with mildly rapid solidification rates of 10–100 K s^{-1}. Since the Sc and RE elements were supersaturated, the alloys in this study were not

homogenized. The peak-aged tensile strength at room temperature, when compared to that of binary Al-0.3 at. % Sc, was found to be up to 25% greater. The increased strengthening provided by the addition of 0.3 at. % RE element was attributed to an increase in volume fraction, strength and stability of $Al_3(Sc,RE)$ precipitates.

A recent study surveyed six different RE additions to Al-0.06 at.%Sc alloys (Dy, Er, Gd, Sm, Y or Yb) [27]. Additions of 0.02 at.% RE showed partial replacement of the RE elements for Sc in the precipitates. Comparison with binary Al-Sc alloys showed that the additions of Gd and Yb resulted in a higher peak hardness than Al-0.06 at.%Sc but a reduced peak hardness than Al-0.08 at.%Sc.

In this study, we investigate dilute Al-0.06 at.% Sc alloys with microalloying additions of two RE elements (Yb or Gd), which have dissimilar solubilities in Al_3Sc. The pseudo-binary Al_3Sc-Al_3Yb system exhibits complete solubility between these two $L1_2$ intermetallics [19]. In contrast, only 15% of the Sc atoms in the Al_3Sc ($L1_2$) phase can be replaced by Gd, corresponding to a composition of $Al_3(Sc_{0.85}Gd_{0.15})$ [18]. In this article we present the results of a study to determine the effects of microalloying concentrations (50 at. ppm) of Yb or Gd on the microstructures of Al-0.06 at.% Sc alloys. Additionally the creep resistance at 300 °C is also examined and it is demonstrated to be improved by the Yb or Gd microalloying additions.

Experimental procedures

The nominal composition of the alloys studied is Al-0.06 at.% Sc-0.005 at.% RE, where RE = Gd or Yb. This composition was chosen to increase the probability that the Sc and RE atoms are fully dissolved in a single-phase solid-solution, α-Al, during the solutionizing treatment (the maximum solid-solubility of Sc in Al is 0.23 at.% [28], but that of Gd and Yb is imprecisely known [26, 29]). Each alloy was produced by dissolving in a melt of 99.99 at.% pure Al (Fe concentration: 22 at. ppm, Si concentration: 38 at. ppm) small quantities of two master alloys, Al-1.2 at.% Sc and Al-0.30 at.% RE (the latter was produced by arc melting the pure elements). The alloys were melted in a resistively-heated furnace at 750 °C in air using an alumina crucible. After thoroughly stirring to ensure uniform composition, the melt was cast into a graphite mold positioned on a large copper plate to promote directional solidification and a large grain diameter. The solutionization treatment was performed at 640 °C for 72 h in air, after which the alloy was water-quenched to room temperature. Aging was subsequently performed at 300 °C in a salt bath (a mixture of sodium nitrite, sodium nitrate and potassium nitrate) for times less than 5 min and in air for longer times, which was also terminated by water quenching. After homogenization, the alloy composition was verified by three-dimensional local-electrode atom-probe (LEAP) tomography and by direct-coupled plasma mass-spectroscopy analysis (performed by ATI Wah Chang Laboratories, Albany, OR); the results are listed in Table 1. The Sc concentration is somewhat higher in the Al–Sc–Gd alloy than the Al–Sc–Yb alloy, but within single significant digit accuracy, the alloys have the same composition (Al-0.06 at.% Sc-0.005 at.% RE, hereafter abbreviated as Al–Sc–RE). Grain boundaries were revealed by etching for 30 s in Poulton's etchant

Table 1 Alloy compositions, precipitate number densities, and mean precipitate radii for Al–Sc–RE, Al–Sc–Zr [12], and Al–Sc [47] alloys for different aging times at 300 °C

Alloy/Aging treatment	Sc concentration (at. ppm)		RE concentration (at. ppm)		Precipitate number density (m^{-3})	Precipitate mean radius (nm)
	Bulk[a] analysis	LEAP[b] analysis	Bulk[a] analysis	LEAP[b] analysis		
Al–Sc–Yb/4 h—300 °C	540	573	80	40	$(2.3 \pm 0.9) \times 10^{22}$	3.2 ± 0.7
Al–Sc–Yb/24 h—300 °C	540	573	80	40	$(1.2 \pm 0.2) \times 10^{22}$	3.4 ± 0.7
Al–Sc–Gd/4 h—300 °C	630	610	50	50	$(8.6 \pm 0.9) \times 10^{22}$	2.1 ± 0.4
Al–Sc–Gd/24 h—300 °C	630	610	50	50	$(1.3 \pm 0.2) \times 10^{23}$	1.8 ± 0.4
Al–Sc/24 h—300 °C	570	575	–	–	$(9 \pm 2) \times 10^{20}$ [d]	8.5 ± 0.6
Al–Sc/66 h—275 °C	570	575	–	–	$(5 \pm 1) \times 10^{22}$ [d]	4.1 ± 0.3
Al–Sc–Zr/72 h—300 °C	600[c]	–	50[c] (Zr)	–	$(9 \pm 1) \times 10^{22}$ [d]	3.3 ± 0.2
Al–Sc–Zr/5 h—300 °C + 4.75 h—400 °C	600[c]	–	50[c] (Zr)	–	$(2 \pm 1) \times 10^{22}$ [d]	5.9 ± 0.3

[a] Chemical analysis performed by ATI Wah Chang Laboratories. Error for Sc is 25 at. ppm and the error for RE elements is 10 at. ppm

[b] Error for the 3D-LEAP analyses is 6 at. ppm for Sc and ± 4 at. ppm for the RE, although a much smaller volume is sampled

[c] Chemical analysis performed by Luvak Inc

[d] Calculated from radius and volume fraction

(2 mL HF, 3 mL HCl, 20 mL HNO_3, 175 mL water) and the grain diameters were found to be greater than 1 mm.

Vickers microhardness measurements were performed at room temperature using a 200 g load on acrylic-mounted samples ground to a 1 μm surface finish. Ten measurements were performed on each sample. Compression creep samples were machined into cylinders with an 8 mm diameter and a 16 mm length. Prior to creep testing, the Al–Sc–RE samples were homogenized and aged for 24 h at 300 °C to produce precipitates with the specified radius. To ensure uniform temperature during creep testing, the samples were allowed to soak at 300 °C for 2 h prior to loading. Tests were performed in a nickel-based superalloy compression cage and the sample ends were lubricated with boron nitride to reduce friction between the cage and the sample. The displacement was measured with a linear variable differential transducer connected to an extensometer. Sufficient time was allowed to reach a minimum strain-rate for each successively higher load applied to the sample. The creep experiments were terminated when a sample achieved 10% strain.

Sample blanks for 3D LEAP tomography were produced by grinding mechanically material to a square cross-section of ca. 300×300 μm^2, after which an atomically sharp tip was created by electropolishing. Initial electropolishing was performed using a solution of 10 vol.% perchloric acid in acetic acid and the final electropolishing was performed using a solution of 2 vol.% perchloric acid in butoxyethanol. 3D LEAP tomography was performed using a LEAP 3000 tomograph (Imago Scientific Instruments, Madison, Wisconsin) [30] operated at a specimen temperature of 30 K, at a pulse frequency of 200 kHz, and a 20% pulse fraction (pulse voltage divided by steady-state dc voltage). Proximity histogram plots (proxigrams) [31] were calculated employing the APEX [32] or IVAS (Imago Scientific Instruments) software programs, using an isoconcentration surface of 7 at.% Sc. The average precipitate composition was determined by counting the number of atoms of each species in the precipitates with the interface position set at the inflection point on the Sc concentration profile. The volume fraction of $L1_2$ precipitates was calculated from the 3D LEAP tomographic data sets by determining the fraction of atoms in the precipitates in a given total volume. The average precipitate radius was calculated from 3D LEAP tomographic data sets using the envelope method [33, 34].

Results

Hardness measurements

After 4 h of aging at 300 °C, both alloys have achieved, within experimental error, their peak hardness values (Fig. 1). These values, when compared to the original quenched and unaged microhardness value, are higher by a factor of 2.2 for Al–Sc–Yb and 2.6 for Al–Sc–Gd. Figure 1 also demonstrates that Al–Sc–Yb hardens at a faster rate than Al–Sc–Gd: the incubation time for the increase in hardness for Al–Sc–Yb is less than the shortest measured aging time of 30 sec, while Al–Sc–Gd has an incubation time of about 10 min. Finally, both Al–Sc–RE alloys exhibit a hardness decrease due to overaging at the longest aging time of 16 days (384 h).

3D Local-Electrode Atom-Probe (LEAP) tomographic results

Three-dimensional reconstructions of LEAP tomographic data (Fig. 2) demonstrate that both Al–Sc–RE alloys achieve high number densities of nano-size precipitates at the peak aging time of 4 h. The precipitate number density for the Al–Sc–Gd alloy, $(8.6 \pm 0.9) \times 10^{22}$ m^{-3}, is found to be about four times higher than for the Al–Sc–Yb alloy, (2.3 ± 0.9)

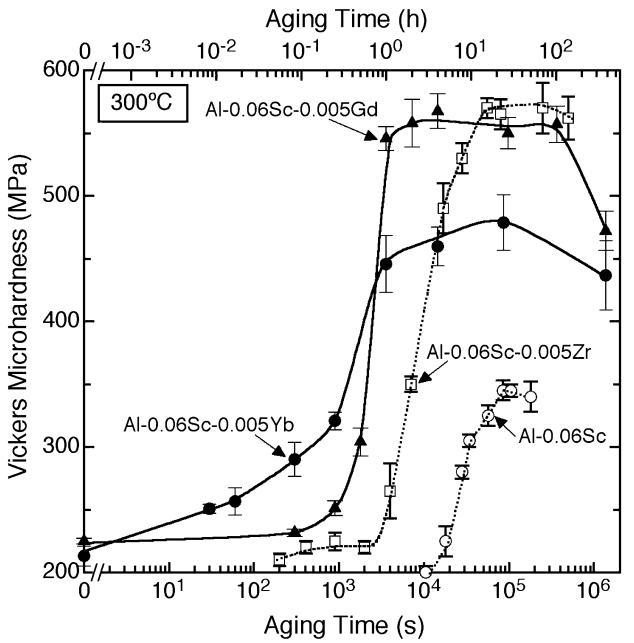

Fig. 1 Vickers microhardness (MPa) versus aging time (seconds) at 300 °C for the Al-0.06 at% Sc-0.005 at.% Yb and Al-0.06 at.% Sc-0.005 at.% Gd alloys. Literature data for Al-0.06 at.% Sc [47] and Al-0.06 at%Sc-0.005 at.% Zr [12] alloys are also displayed for comparison

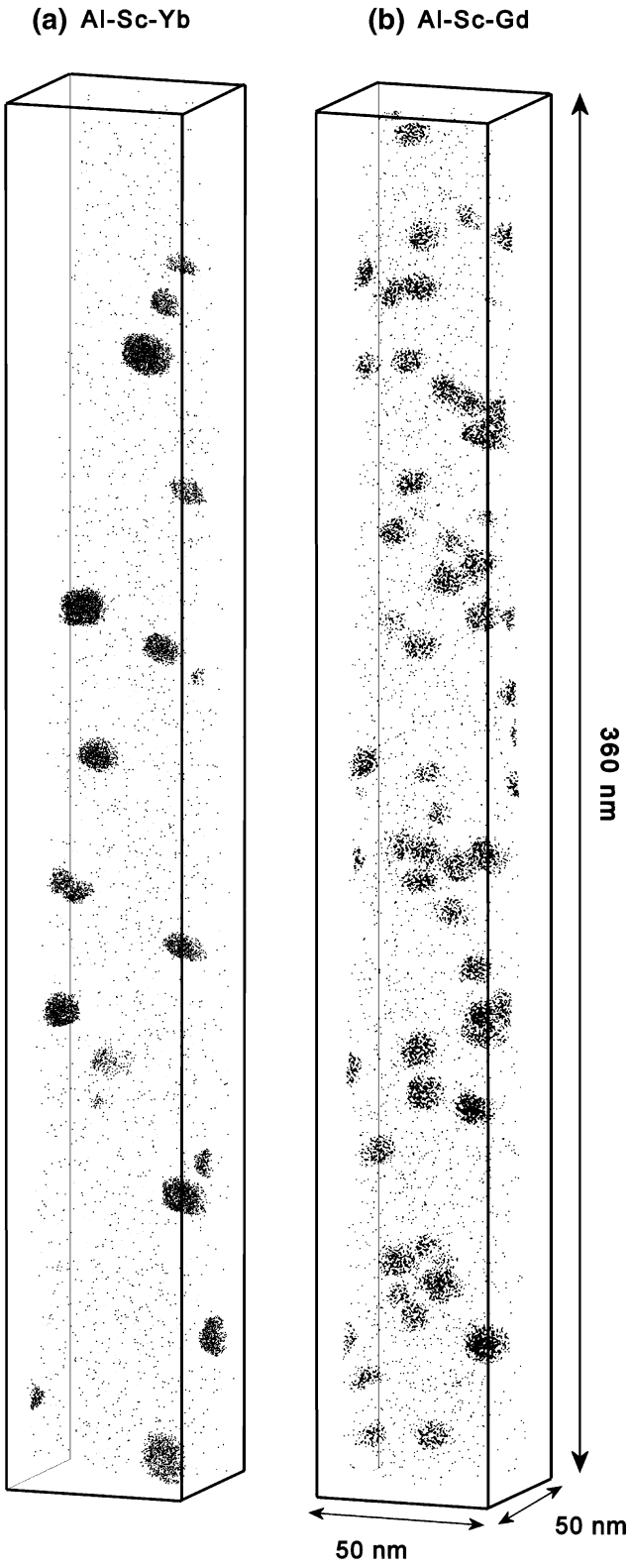

Fig. 2 3D LEAP tomographic reconstructions for: (**a**) Al–Sc–Yb; and (**b**) Al–Sc–Gd. Each alloy was peak-aged for 4 h at 300 °C and each data set contains 15 million atoms. Only Sc atoms are displayed for the sake of clarity

$\times 10^{22}$ m^{-3} (Table 1). The average precipitate radius is somewhat smaller for the Al–Sc–Gd alloy as compared to the Al–Sc–Yb alloy (2.1 ± 0.4 nm versus 3.2 ± 0.7 nm, respectively). A second factor contributing to the higher number density in the Al–Sc–Gd alloy is that the volume fraction of precipitates is slightly lower for the Al–Sc–Yb alloy (0.21 ± 0.01%) than for the Al–Sc–Gd alloy (0.25 ± 0.01%). The precipitate volume fraction can also be calculated from the overall composition by subtracting the solute content in the matrix after aging (found by 3D LEAP tomographic measurements of the aged alloys) from the overall solute content in the as-homogenized state (also found by 3D LEAP tomographic measurement), assuming that the amount of solute no longer in the matrix has formed the precipitate phase with the stoichiometric composition. The actual concentration of Sc plus RE in the precipitates is found to be slightly greater than the stoichiometric composition at 27.0% for Al–Sc–Yb and 26.8% for Al–Sc–Gd, which is, however, most likely a field-evaporation effect that has been observed previously for Al_3Zr precipitates in Al [35] and Al_3Sc precipitates [36]. When using the matrix compositions, similar volume fractions are obtained (0.22 ± 0.01% for Al–Sc–Yb and 0.25 ± 0.01% for Al–Sc–Gd), confirming the accuracy of the direct 3D LEAP tomographic measurement of volume fraction.

The proxigrams after peak-aging (4 h) are displayed in Figs. 3 and 4 and reveal additional differences between the two alloys. For the Al–Sc–Yb alloy (Fig. 3), the average Yb concentration in the precipitates is 3.3 at.%, corresponding to $Al_3(Sc_{0.87}Yb_{0.13})$. In the $L1_2$ precipitate cores, however, the Yb concentration achieves a concentration as high as 11 at.%. The proxigram for the Al–Sc–Gd alloy (Fig. 4) exhibits a lower average RE element precipitate concentration of 1.4 at.% Gd, corresponding to $Al_3(Sc_{0.94}Gd_{0.06})$. The Gd atoms are also more uniformly distributed within the precipitates than the Yb atoms in the Al–Sc–Yb alloy. Upon further aging to 24 h, the average precipitate radius and number density remain almost constant within experimental error (Table 1). The average concentration, however, of Yb and Gd in the precipitates increases to 3.7% and 2.0%, respectively (Figs. 3, 4). This is a 12% and 43% increase, respectively, in RE concentration in the precipitates over the 4 h aging time.

Radial Distribution Functions (RDF)

The hardness of the Al–Sc–Yb alloy (Fig. 1) increases at an earlier aging time than it does for the Al–Sc,

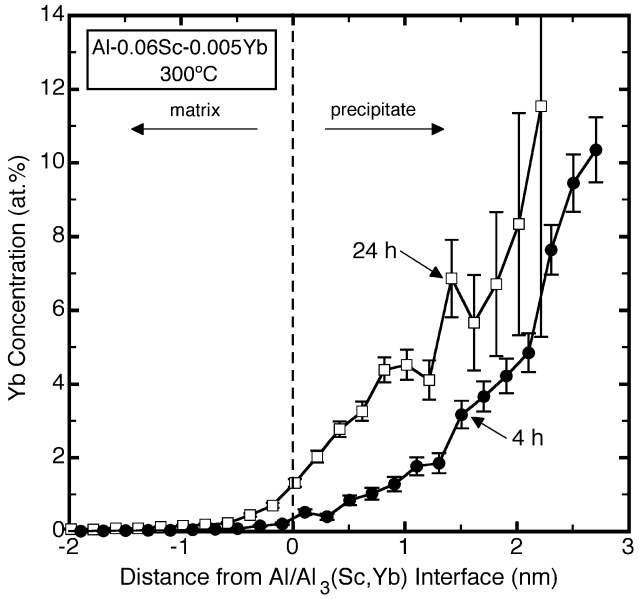

Fig. 3 Proxigrams showing the Yb concentration (at.%) as a function of radial distance (nm) from the α-Al/Al_3(Sc,Yb) heterophase interface ($x = 0$) for Al–Sc–Yb aged for 4 and 24 h at 300 °C

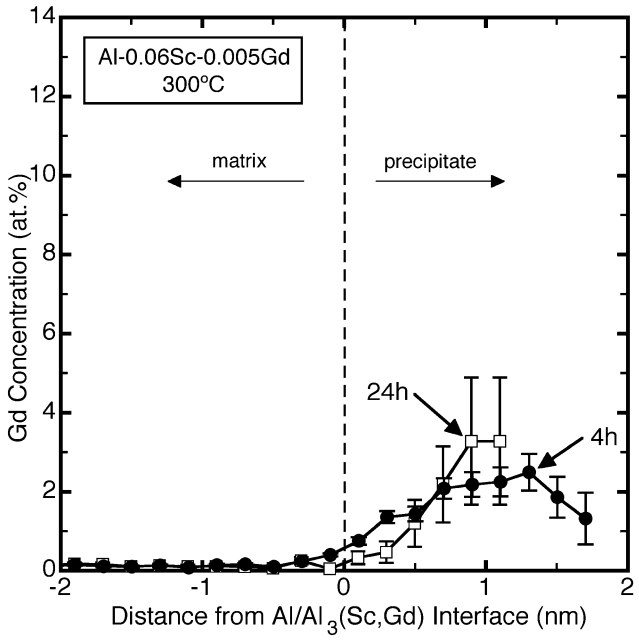

Fig. 4 Proxigrams showing the Gd concentration (at.%) as a function of radial distance (nm) from the α-Al/Al_3(Sc,Gd) heterophase interface ($x = 0$) for Al–Sc–Gd aged for 4 and 24 h at 300 °C

Al–Sc–Zr and Al–Sc–Gd alloys. This initial rapid increase in hardness indicates the presence of either short-range order clusters and/or some precipitation at these early aging times. In the three-dimensional reconstruction of the LEAP tomographic data there is no clear evidence of visible precipitates at an aging time of 15 min (Fig. 5). It is difficult to evaluate the state of clustering from Fig. 5 by the procedure used by Schmuck et al. [37–39]. Therefore to examine the early stages of precipitation in more detail, a radial distribution function (RDF) analysis [40, 41] was employed to evaluate the presence of solute clustering in the Al–Sc–Yb alloy in the homogenized state and after 15 min of aging. An important advantage of performing an RDF analysis using 3D LEAP tomography is that the analysis is performed in direct space, whereas scattering (X-ray or neutron) experiments are performed in reciprocal space and this implies that the results need to be deconvolved to obtain direct space information. The standard definition of an RDF [42] at a given radial distance is defined as the average concentration of component i around a given solute species X, when summed over all of the atoms of type X, and is given by:

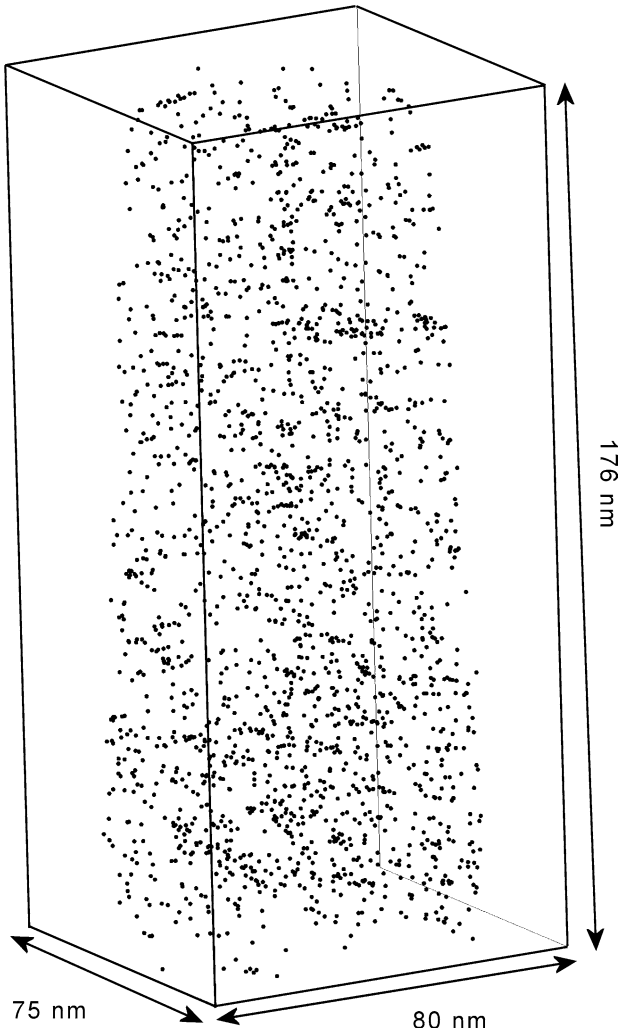

Fig. 5 3D LEAP tomographic reconstruction for the Al–Sc–Yb alloy aged for 15 min at 300 °C, where only the Yb atoms are shown for the sake of clarity. This data set contains 19 millions atoms

$$\mathrm{RDF} = \frac{\langle C_i^{\mathrm{X}}(r)\rangle}{C_i^{\mathrm{o}}} = \frac{1}{C_i^{\mathrm{o}}}\sum_{k=1}^{N_{\mathrm{X}}}\frac{N_i^k(r)}{N_{\mathrm{tot}}^k(r)}$$

where C_i^{o} is the overall concentration of element i in the alloy, $C_i^{\mathrm{X}}(r)$ is the concentration of component i at a distance r from component X, $N_{\mathrm{tot}}^k(r)$ is the total number of atoms in the shell at a distance r from the k^{th} atom of type X, $N_i^k(r)$ is the number of atoms of type i in the shell at a distance of r from the k^{th} atom of type X. The RDF plot of the data for the 15 min aging time (Fig. 6b) demonstrates that the partial RDF for Yb–Yb reaches a maximum of 32, indicating that, at a given distance from a Yb atom, there is 32 times the concentration expected from a random distribution of Yb atoms at the second nearest-neighbor position. The partial RDF for a perfectly random distribution of atoms corresponds to a value of unity and is given by the horizontal lines in Fig. 6a, b. For the initially homogenized state, Fig. 6a, the partial RDF for Yb–Yb is ca. 4.5 at the second nearest-neighbor position, which implies that it is a factor of ca. 7 smaller than after 15 min of aging. Figure 6a, b taken in concert indicates that much of the clustering of Yb atoms has occurred during this 15 min aging period.

High-temperature creep experiments

Figure 7 demonstrates that both Al–Sc–RE alloys exhibit creep behavior at 300 °C characterized by a high apparent stress exponent of 29–37, which is indicative of the presence of a threshold stress, σ_{th}, below which the creep rate, $\dot{\varepsilon}$, cannot be experimentally measured [43]. The power-law creep equation including a threshold stress is:

$$\dot{\varepsilon} = A(\sigma - \sigma_{\mathrm{th}})^n \exp\left(-\frac{Q}{R_g T}\right) \quad (2)$$

where A is the Dorn constant, σ is the applied stress, Q is the activation energy of creep in pure Al, $n = 4.4$ is the stress exponent of pure Al [44], and R_{g} is the ideal gas constant. By plotting $\dot{\varepsilon}^{1/n}$ versus σ [45], threshold stresses of 24 MPa for Al–Sc–Gd and 33 MPa for Al–Sc–Yb are calculated.

Discussion

Hardness Measurements and Strength

Both of the present Al-0.06 at.%Sc-0.005 at.%RE alloys had similar microhardness behavior to Al-0.06 at.%Sc-0.02 at.%RE alloys studied previously [27]. Both of the Gd containing alloys (with 50 or 200 ppm) showed a similar incubation time to the binary Al-0.08 at.%Sc. The Yb containing alloys both showed a rapid increase in the hardness at much shorter aging times than the binary alloys. All of the alloys containing either 50 or 200 ppm of Gd or Yb were stronger than the binary Al-0.06 at.%Sc but did not attain the hardness of the Al-0.08 at.%Sc. In both Al–Sc–RE alloys, the large increase in hardness in the peak-aged condition

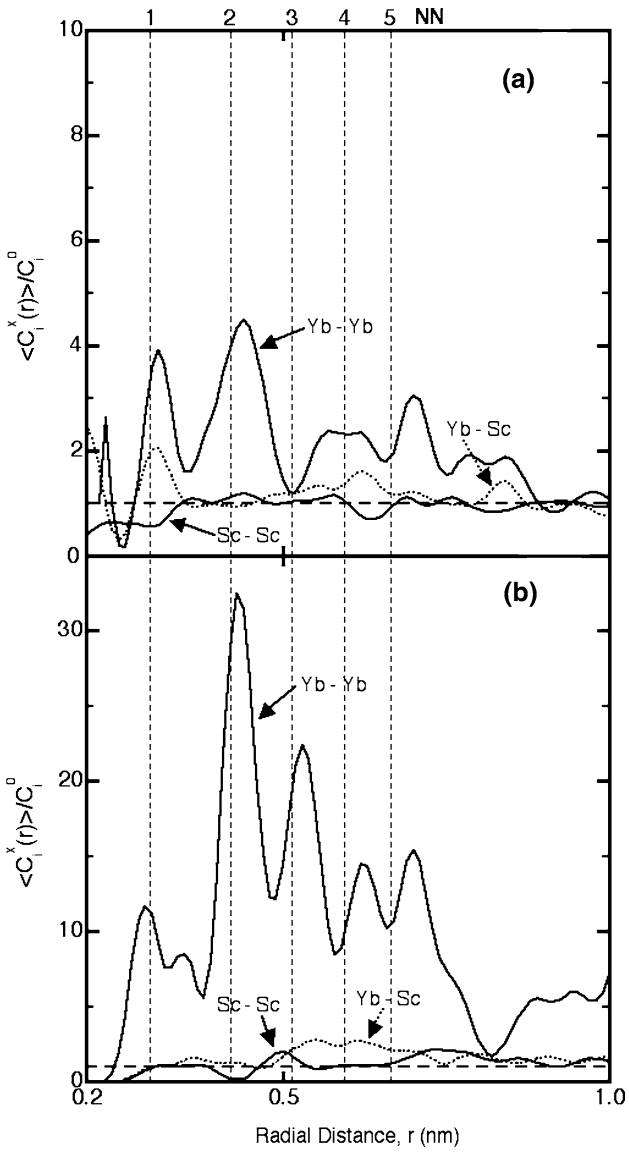

Fig. 6 Experimental partial radial distribution functions (RDFs) for Al–Sc–Yb in: (**a**) the homogenized state; and (**b**) aged for 15 min at 300 °C, showing the radial distance (nm) of the second element with respect to the central first element. The dashed horizontal line at unity indicates the value expected for a completely random distribution of solute atoms. Vertical lines indicate the first to fifth nearest-neighbor (NN) distances for Al_3Yb

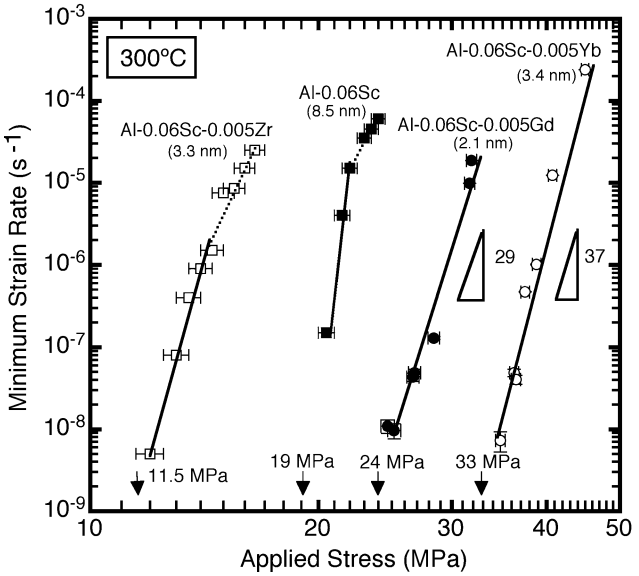

Fig. 7 Double logarithmic plot of minimum strain rate (s^{-1}) versus applied stress (MPa) for creep at 300 °C of Al–Sc–Yb and Al–Sc–Gd, as well as Al–Sc [47] and Al–Sc–Zr [12], with precipitate radii given in parentheses. Threshold stresses are marked as vertical arrows along the applied stress axis

as compared to the homogenized state (Fig. 1) is attributed to the formation of a high number-density of $Al_3(Sc_{1-x}RE_x)$ precipitates (Table 1 and Fig. 2). For the Al–Sc–Yb the peak number density is $(2.3 \pm 0.9) \times 10^{22}$ m^{-3} at 4 h, and for Al–Sc–Gd it is $(1.3 \pm 0.2) \times 10^{23}$ m^{-3} at 24 h at 300 °C. Figure 8 displays the yield stress increment for both alloys as a function of precipitate radius after aging for 4 and 24 h at 300 °C, respectively. The yield stress increment is calculated by taking the increase in microhardness (homogenized value subtracted from aged value) and dividing by a factor of 3 to convert from hardness to yield stress [46]. Calculated curves are shown for three strengthening mechanisms: (i) Orowan strengthening, where dislocations bypass the precipitates; (ii) order strengthening, where dislocations shear the precipitates; and (iii) coherency and modulus strengthening, where dislocations are repelled by the precipitates (before shearing occurs) due to the mismatch in elastic modulus and lattice parameter between the matrix and precipitate phases. The same analysis was previously performed for dilute Al–Sc alloys [47] and Al–Sc–Zr alloys [12], and we utilize the same equations as in Ref. [12] with the lattice parameter mismatch at ambient temperature given by 1.46% for Al–Sc–Gd and 1.64% for Al–Sc–Yb. Vegard's law was assumed and used to calculate the average lattice parameters of the precipitates after peak aging for 4 h, based on the composition dependence of the lattice parameter of $Al_3(Sc_{1-x}RE_x)$ [18, 19] and assuming a spatially uniform distribution of the RE element in the precipitates.

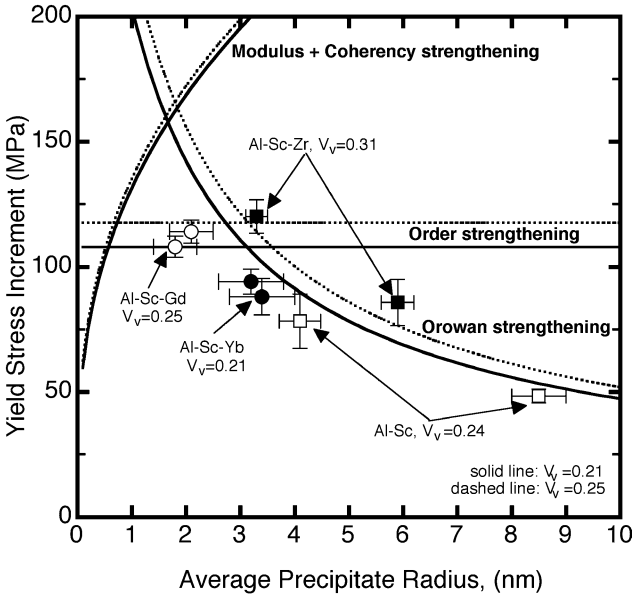

Fig. 8 Yield stress increment (MPa) calculated from microhardness versus average precipitate radius (nm) for Al–Sc–Yb and Al–Sc–Gd. Literature values for Al–Sc [47] and Al–Sc–Zr [12] are also displayed. The solid and dashed lines represent the theoretical strength increments for the three possible strengthening mechanisms calculated using the equations in Ref. [12] for the volume fractions, V_v, of the Al–Sc–RE alloys at peak aging

The dashed lines in Fig. 8 represent the three strengthening contributions calculated for the larger volume fraction of 0.25% in the Al–Sc–Gd alloy, while the smaller volume fraction in the Al–Sc–Yb alloy of 0.21% (solid lines) leads to somewhat smaller strength values. Mechanism (i) occurs in parallel with mechanisms (ii) and (iii), which are in series with each other. From Fig. 8, it is then predicted that order strengthening controls strength at the lowest precipitate radii (to 0.7 nm), followed by modulus/coherency strengthening (from 0.7 to 1.8 nm), while Orowan strengthening is the controlling strengthening mechanism at larger precipitate radii.

The 3.2–3.4 nm radius precipitates in the Al–Sc–Yb alloy fall in the regime where Orowan strengthening is predicted to be dominant, and there is good agreement between predicted and measured yield stress increment. The 1.8–2.1 nm radii precipitates in the Al–Sc–Gd alloy correspond to the regime where the modulus/coherency strengthening mechanism overlaps with the Orowan mechanism, and the experimental values are lower than the predicted values. This may be due to the non-uniform radius and spatial distribution of the precipitates. For an Al–0.06 at.% Sc-0.005 at.% Zr alloy (previously reported in Ref. [12] and hereafter referred to as Al–Sc–Zr) with an average precipitate radius of 3.3 nm, Fig. 8 demonstrates that the Orowan mechanism is the strength-controlling mechanism. The

same alloy with a larger precipitate radius of 5.9 nm exhibits a decreased strength value, which is consistent with the dominance of the Orowan mechanism. The relatively large average radii (4.1 and 8.5 nm) of the precipitates in an Al-0.06 at.% Sc alloy (previously reported in Ref. [47] and hereafter referred to as Al–Sc) leads to smaller strength increments. Again, hardness values for both Al–Sc and Al–Sc–Zr are in good agreement with predictions based on the Orowan strengthening mechanism.

Temporal evolution of precipitates

The earlier increase in hardness for the Al–Sc–Yb alloy, which is observed at aging times as short as 30 s (Fig. 1), is attributed to the formation of Yb clusters as demonstrated by the RDF analysis (Fig. 6). Clusters are difficult to detect in a 3D-reconstruction for the 15 min aging time (Fig. 5) but are quantified by the RDF diagrams displayed in Fig. 6. Furthermore, the large positive oscillation at the second nearest-neighbor distance in the Yb–Yb partial RDF and the relatively small value at the first nearest-neighbor distance in these curves indicate the possibility of short-range order. Indeed, the Yb atoms are expected to be at the second nearest-neighbor distance in Al_3Yb ($L1_2$ structure), but not at the first nearest-neighbor distance. Partial RDFs for Yb–Sc and Sc–Sc pairs display values significantly closer to unity (no higher than 2.8 for Yb–Sc and 2.2 for Sc–Sc), indicating that the clustering of Sc is much less significant at 15 min of aging.

While no experimental data for the diffusivity of Yb in Al was found in the literature, Fig. 6 implies that Yb diffuses significantly faster than Sc in Al at 300 °C, and that Yb-rich clusters form within minutes of aging at this temperature, thereby increasing markedly the hardness of the alloy (Fig. 1). After 4 h of aging (Figs. 2a, 3), the precipitates consist of a Yb-rich core surrounded by a Sc-rich spherical shell, which is reminiscent of the Al–Sc–Ti [17], Al–Sc–Zr [9, 10, 13, 16, 48], Al–Li–Sc [49], Al–Li–Ti [50], Al–Li–Zr [51, 52] and Al–Li–Hf [53] systems. For the Al–Sc–Ti, Al–Sc–Zr and Al–Li–Sc alloys the Sc is in the core, while for the Al–Sc–RE alloys the Sc is in the shell. This indicates that the slower-diffusing Sc subsequently diffuses toward the Yb-rich precipitates formed at early aging times. The Sc/Yb ratio of 7 measured in the precipitates for the 4 h peak-aged alloy is somewhat lower than the overall alloy elemental ratio measured by 3D-LEAP tomographic analyses in the homogenized and quenched alloy. However, the matrix concentration of Sc after 4 h of aging, as measured by 3D-LEAP tomography, is 100 ± 3 at. ppm, higher than the equilibrium solubility of Sc in Al in the binary alloy, which is 20 ± 6 at. ppm, as calculated from 3D-LEAP tomographic data at longer aging times.

The Yb-rich core obtained after 4 and 24 h of aging indicates that diffusion does not homogenize the precipitates for these aging times. This may be due to the small diffusivity of Yb and Sc in $Al_3(Sc,Yb)$, as expected from the high melting point of Al_3Sc (1,320 °C) and the lower atomic mobility in ordered alloys as compared to disordered alloys because of correlation effects. The Yb enrichment towards the precipitate center may also be linked to the increase in lattice parameter of $Al_3(Sc,Yb)$ with increasing Yb concentration [19], which exacerbates the lattice parameter mismatch with the α-Al matrix and concomitantly the elastic strain energy. Similarly, the slight Gd enrichment in the precipitate cores of the Al–Sc–Gd alloy (Fig. 4) may be also be due to an increase in lattice parameter mismatch with the substitution of Gd for Sc in Al_3Sc [18]. This enrichment of Gd in the center of the precipitates was even more pronounced in a recent study involving an Al-0.06 at.%Sc alloy with a higher concentration of Gd (200 ppm) [27]. In this alloy, the concentration of Gd in the center of the precipitates reached 7 % after 24 h, higher than the 3.3 % achieved in the present study with 50 ppm of Gd. In this study, an even stronger enrichment of Er was found in the precipitate core (16 at.%).

The Al–Sc–RE alloys contain smaller precipitates as compared to the binary Al–Sc alloy, which is in qualitative agreement with their more rapid precipitation kinetics at 300 °C; peak hardness is achieved after ca. 4 h for the ternary Al–Sc–RE alloys, as compared to 24 h for the binary Al–Sc alloy. The precipitation kinetics of the Al–Sc–Zr alloy is somewhat slower than those of the Al–Sc–RE alloys, achieving peak hardness after 16 h at 300 °C, most likely due to the smaller diffusivity of Zr in Al. The larger number density, smaller average precipitate radius, and more rapid precipitation kinetics in the Al–Sc–RE alloys compared with the Al–Sc alloy indicates that the RE elements, even for the microalloying concentrations investigated in this study, have a considerable effect on the nucleation and growth kinetics of the precipitates. The differences are explainable by the different nucleation currents in the two alloys, which are a result of the different heterophase interfacial free energies and supersaturations of solute species. The exact heterophase interfacial free energy values for these alloys are, however, unknown, and the Sc, Gd, or Yb supersaturations cannot be calculated because the ternary phase diagrams in the relevant regions are unknown. It is also possible that the increased number density of

precipitates results from RE element clusters serving as heterogeneous nucleation sites for precipitate formation.

Creep properties

Figure 7 demonstrates that microalloying additions of Yb or Gd increase dramatically the creep resistance of the binary Al–Sc alloy. In a previous study, the threshold stress for an Al–Sc alloy with 4.1 nm average precipitate radius was 8 MPa [47], or about one quarter of the value of 33 MPa for the Al–Sc–Yb alloy with a similar precipitate radius of 3.4 nm. When compared to Al–Sc–Gd with a threshold stress of 24 MPa, the value of the threshold stress for Al–Sc with 4.1 nm average precipitate radius is about one third. It is known that increasing the precipitate radius in Al-Sc alloys increases the threshold stress [8, 12, 23, 47]. Despite this fact, in Fig. 7 is displayed the creep data for the Al–Sc alloy with 8.5 nm radius precipitates [47] which, when compared to the Al–Sc–RE alloys with significantly smaller (2.1–3.4 nm radius) precipitates, still has threshold stresses 1.3–1.7 times lower. In comparison to an Al–Sc–Zr alloy with similar composition and precipitate radius [12], the Al–Sc–RE alloys display threshold stresses that are 2–3 times greater (Fig. 7).

The remarkable increase in threshold stress displayed by the Al–Sc–RE alloys may be due to the known increased lattice parameter mismatch between the α-Al matrix and the $Al_3(Sc_{1-x}RE_x)$ precipitates [19] as compared to Al_3Sc or $Al_3(Sc_{1-x}Zr_x)$ [22]. An increase in threshold stress with increasing lattice parameter mismatch was recently predicted by a model which considered the elastic effects on climb of dislocations over precipitates [23]. This model, as well as experimental results [8, 12, 47], indicate that increasing the mean precipitate radius increases the threshold stress normalized by the Orowan stress. Thus, it should be possible to achieve even higher values of the threshold stress for Al–Sc–RE alloys if precipitate radii are coarsened beyond the current values of 3.4 nm and remain coherent or semi-coherent with the matrix.

Conclusions

The nanostructure and mechanical properties of two Al-0.06 at.% Sc alloys microalloyed with 0.005 at.% (50 at. ppm) Yb or Gd are studied. Upon aging at 300 °C, both alloys harden by formation of nanosize, coherent $Al_3(Sc_{1-x}RE_x)$ ($L1_2$) precipitates, but they exhibit dissimilar precipitation kinetics resulting in both different microstructures and temporal evolution of the hardness.

- When compared to the binary Al–Sc alloy, the Al–Sc–RE alloys show an increase in peak microhardness values and decrease in aging times to reach peak hardness. This is due to a higher number density of precipitates, or equivalently, to a smaller precipitate radius at peak hardness.
- The Al–Sc–Gd alloy attains a higher peak hardness (by 90 MPa) compared to the Al–Sc–Yb alloy, due to a fourfold increase in precipitate number density.
- Both Gd and Yb segregate to the precipitate phase. At peak hardness, the average RE elemental concentration in the precipitates is more than twice as large for Al–Sc–Yb as it is for Al–Sc–Gd, 3.3 versus 1.4 at.%, respectively.
- The Al–Sc–Yb alloy exhibits an earlier onset of hardening than the Al–Sc–Gd alloy, due to the formation of Yb-rich clusters, which are originally free of Sc (as determined by 3D LEAP tomography for an aging time of 15 min employing a radial distribution function analyses). This indicates that the diffusivity of Yb is greater than that of Sc in this alloy.
- In Al–Sc–Yb (and to a lesser extent in Al–Sc–Gd), the RE is more concentrated in the center of the precipitates than at the heterophase interface. For the Al–Sc–Yb alloy, this can be interpreted as Yb first forming $Al_3(Yb_{1-x}Sc_x)$ precipitates, followed by subsequent Sc partitioning to the precipitates as they grow. For both Gd and Yb, a further possible cause for the RE enrichment in the center of the precipitates is the minimization of lattice parameter mismatch with the matrix, which is increased by the presence of RE elements in the precipitates.
- Both Al–Sc–RE alloys have much improved creep resistance when compared to binary Al–Sc or ternary Al–Sc–Zr alloys with the same composition and precipitate radius. The observed increase in threshold stress is thought to result from the increase in lattice parameter mismatch produced by the RE element in the precipitates, which affects the dislocations bypassing the precipitates.

Acknowledgements This research was supported by the United States Department of Energy through grant DE-FG02–98ER45721. Atom-probe tomographic measurements were performed at the Northwestern University Center for Atom-Probe Tomography (NUCAPT), using a LEAP tomograph purchased with funding from the NSF-MRI (DMR-0420532, Dr. Charles Bouldin monitor) and ONR-DURIP (N00014–0400798, Dr. Julie Christodoulou monitor) programs. The authors thank Richard Karnesky and Keith Knipling (Northwestern University) for helpful discussions.

References

1. Hyland RW (1992) Metall Trans A 23A:1947
2. Toropova, LS, Eskin DG, Kharakterova ML, Dobatkina TV, Advanced Aluminum Alloys Containing Scandium. Gordon & Breach, 1998
3. Novotny GM, Ardell AJ (2001) Mater Sci Eng A A318:144
4. Marquis EA, Seidman DN (2001) Acta Mater 49:1909
5. Royset J, Ryum N (2005) Int Mater Rev 50(2):1
6. Knipling KE, Dunand DC, Seidman DN (2006) Zeitschrift Metallkunde 97(3):246
7. Marquis EA, Seidman DN, Asta M, Woodward C, Ozolins V (2003) Phys Rev Lett 91:36101
8. Marquis EA, Seidman DN, Dunand DC (2003) Acta Mater 51:4751
9. Fuller, CB, Ph.D Thesis (2003) Northwestern University; http://arc.nucapt.northwestern.edu/refbase/show.php?record = 147; as on July 5, 2006
10. Fuller CB, Murray JL, Seidman DN (2005) Acta Mater 53:5401
11. Fuller CB, Seidman DN (2005) Acta Mater 53:5415
12. Fuller CB, Seidman DN, Dunand DC (2003) Acta Mater 51:4803
13. Forbord B, Lefebvre W, Danoix F, Hallem H, Marthinsen K (2004) Scripta Mater 51:333
14. Clouet E, Nastar M, Barbu A, Sigli C, Martin G (2005) Solid–Solid Phase Transformations in Inorganic Materials TMS 1
15. Hallem H, Lefebvre W, Forbord B, Danoix F, Merthinsen K (2006) Mater Sci and Eng A 421(1–2):154
16. Tolley A, Radmilovic V, Dahmen U (2005) Scripta Mater 52:621
17. van Dalen ME, Dunand DC, Seidman DN (2005) Acta Mat 53:4225
18. Zalutskaya OI, Kontseyoy VG, Karamishev NI, Ryabov VR, Zalutskii II, Dopovidi Akademii Nauk Ukr RSR (1970) 751
19. Palenzona AJ (1972) J Less-Common Metals 29:289
20. Mondolfo LF (1976) Aluminum alloys: structure and properties. Butterworths, London
21. Bergner D, Chi NV (1977) Wissenschaftliche Zeitschrift der Padagogischen Hochschule ''Krupskaja NK'', Halle XV, Heft 3
22. Harada Y, Dunand DC (2002) Mater Sci Eng A 329–331:686
23. Marquis EA, Dunand DC (2002) Scripta Mater 47:503
24. Sawtell RR, Morris JW (1988) Proc Dispersion Strengthened Aluminum Alloys. TMS, Warrendale, PA, p 409
25. Sawtell RR (1988) Exploratory alloy development in the system Al–Sc–X PhD Thesis. University of California, Berkeley
26. Massalski, Binary Alloy Phase Diagrams (1990) (ASM Int.,)
27. Karnesky RA, Van Dalen ME, Dunand DC, Seidman DN (2006) Scripta Mater 55:437
28. Murray JL (1998) J Phase Equil 19(4):380
29. Kononenko VI, Golubev SV (1990) Russian Metall 2:197
30. Kelly TF, Gribb TT, Olson JD, Martens RL, Shepard JD, Wiener SA, Kunicki TC, Ulfig RM, Lenz DR, Strennen EM, Oltman E, Bunton JH, Strait DR (2004) Micros Microanal 10:373
31. Hellman OC, Vandenbroucke JA, Rüsing J, Isheim D, Seidman DN (2000) Micros Microanal 6:437
32. Hellman OC, Vandenbroucke J, du Rivage JB, Seidman DN (2002) Mater Sci Eng A 327(1):29
33. Miller MK (2000) Atom probe tomography: analysis at the atomic level. Kluwer Academic, New York
34. Hyde JM, English CA (2001) Proc MRS Fall 2000 Meeting 650:1
35. Knipling, KE (2006) Ph.D Thesis, Northwestern University
36. Marquis EA Seidman DN, Asta M, Woodward C (2006) Acta Mater 54:119
37. Schmuck C, Caron P, Hauet A, Blavette D (1997) Phil Mag A 76(3):527
38. Schmuck C (1997) Ph.D Thesis, Univeristy of Rouen
39. Sudbrack C, Decomposition behavior in model Ni-Al-Cr-X superalloys : temporal evolution and compositional pathways on a nanoscale. 2004, Ph.D Thesis, Northwestern University: http://arc.nucapt.northwestern.edu/refbase/show.php?record = 16; as on July 5, 2006
40. Sudbrack CK, Noebe RD, Seidman DN (2006) Phys Rev B 73:212101
41. De Geuser F, Lefebvre W, Blavette D (2006) Phil Mag Lett 86(4):227
42. Ziman JM (1979) Models of disorder: the theoretical physics of homogeneously disordered systems. Cambridge University Press, Cambridge
43. Cadek J (1988) Creep in metallic materials. Elsevier, New York
44. Frost HJ, Ashby MF (1982) Deformation-mechanism maps: the plasticity and creep of metals and ceramics. Pergamon, Oxford
45. Lagneborg R, Bergman B (1976) Metal Sci 10:20
46. Tabor D (1956) Br J App Phys 7:159
47. Marquis EA, Seidman DN, Dunand DC (2002) Acta Mater 50:4021
48. Clouet E, Lae L, Epicier T, Lefebvre W, Nastar M, Deschamps A (2006) Nature Mater 5:482
49. Miura Y, Horikawa K, Yamada K, Nakayama M (1994) Aluminum Alloys: Their Phys Mech Prop 2:161
50. Di Z, Saji S, Fujitani W, Hori S (1987) Trans Japan Inst Metals 28(10):827
51. Gayle FW, Vander Sande JB (1984) Scripta Met 18:473
52. Yuan GS, Zhao ZY, Zhu XD, Kuang JP, Liu Y, Xing ZJ (1991) Mat Sci Eng A 134:1179
53. Norman AF, Tsakiropoulos P (1991) Mat Sci Eng A 134:1144